Photoelectron spectroscopic and computational studies of the $Pt@Pb_{10}^{1-}$ and $Pt@Pb_{12}^{1-/2-}$ anions

Andrej Grubisic[a], Haopeng Wang[a], Xiang Li[a], Yeon-Jae Ko[a], F. Sanem Kocak[b], Mark R. Pederson[c,1], Kit H. Bowen[a,1], and Bryan W. Eichhorn[b,1]

[a]Departments of Chemistry and Materials Science, Johns Hopkins University, Baltimore, MD 21218; [b]Department of Chemistry and Biochemistry, University of Maryland, College Park, MD 20742; and [c]Center for Computational Materials Science, Naval Research Laboratory, Washington, DC 20375

Edited by Tobin J. Marks, Northwestern University, Evanston, IL, and approved July 22, 2011 (received for review April 29, 2011)

A combination of anion photoelectron spectroscopy and density functional theory calculations has elucidated the geometric and electronic structure of gas-phase endohedral Pt/Pb cage cluster anions. The anions, $Pt@Pb_{10}^{1-}$ and $Pt@Pb_{12}^{1-}$ were prepared from "preassembled" clusters generated from crystalline samples of $[K(2,2,2\text{-crypt})]_2[Pt@Pb_{12}]$ that were brought into the gas phase using a unique infrared desorption/photoemission anion source. The use of crystalline $[K(2,2,2\text{-crypt})]_2[Pt@Pb_{12}]$ also provided access to $K[Pt@Pb_n]^-$ anions in the gas phase (i.e., the K^+ salts of the $Pt@Pb_n^{2-}$ anions). Anion photoelectron spectra of $Pt@Pb_{10}^{1-}$, $Pt@Pb_{12}^{1-}$, and $K[Pt@Pb_{12}]^{1-}$ are presented. Extensive density functional theory calculations on $Pt@Pb_{10}^{3-/2-/1-/0}$ and $Pt@Pb_{12}^{2-/1-}$ provided candidate structures and anion photoelectron spectra for $Pt@Pb_{10}^{1-}$ and $Pt@Pb_{12}^{1-}$. Together, the calculated and measured photoelectron spectra show that $Pt@Pb_{10}^{1-}$ and $Pt@Pb_{12}^{2-/1-}$ endohedral complexes maintain their respective D_{4d} and slightly distorted I_h symmetries in the gas phase even for the charge states with open shell character. Aside from the fullerenes, the $Pt@Pb_{12}^{2-}$ endohedral complex is the only bare cluster that has been structurally characterized in the solid state, solution, and the gas phase.

endohedral clusters | negative ions | mass spectrometry

The synthesis, characterization, and solution chemistry of the soluble main group polyanions (i.e., Zintl ions) have a 120-y history (1) that has been well reviewed (2–7). The use of soluble Zintl clusters for the preparation of unique materials was pioneered by Haushalter and O'Connor in the 1980s in their work on magnetic spin glasses, electronic materials, and metallic coatings (8–13). Since that time, scientists have pursued new materials utilizing various Zintl ion precursors to both ionically and covalently link the cluster anions into oligomers (14–18), polymers (19, 20), network solids (21–23), and nanomaterials (24–26). Simultaneously, gas-phase chemists have prepared bare (e.g., ligand-free) clusters in molecular beams, studied their size-dependent properties, and explored possible condensed-phased manifestations (27–30). Especially notable was the discovery of C_{60} (31) in molecular beam experiments and its subsequent macroscopic synthesis (32). Several other cluster species (not yet assembled into solids) show unusual gas-phase stability (e.g., metcar cages Ti_8C_{12} and Zr_8C_{12}, refs. 33 and 34, and Al_{13}^{1-}-type cluster anions comprising icosahedral cages of group 13 elements with one atom inside; i.e., $Al@Al_{12}^{1-}$, refs. 27, 35, and 36).

Traditional inorganic cluster compounds are stabilized by ligand spheres that reduce cluster-core interactions. By contrast, bare gas-phase clusters devoid of ligands are vulnerable to coalescence. Combining the attributes of both are salts composed of Zintl cluster anions and their countercations. Not only are Zintl cluster anions ligand free with several structural similarities to gas-phase clusters (e.g., $Pt@Pb_{12}^{2-}$ is isostructural to Al_{13}^{1-} and the As_{20} shell of $As@Ni_{12}@As_{20}^{3-}$ is isostructural to Ti_8C_{12} and C_{20}), but they can also be prepared in macroscopic quantities, fully characterized, and used in subsequent reactions. Several researchers (3, 14, 37–41, 42–48) have prepared and isolated a number of salts of endohedral Zintl anion clusters with unprecedented structures and unique properties; e.g., σ-aromaticity, paramagnetism, and remarkable dynamic exchange processes. These "intermetalloid" clusters (3, 5, 48–51) display structures very different from the corresponding intermetallic solids or the Zintl ion parent compounds, and are viewed as a different class of cluster compounds with properties (e.g., magnetic, electrochemical, optical) that remain largely unexplored. For example, although all four E_{12}^{2-} clusters (E = Si, Ge, Sn, Pb) are predicted to have σ-aromatic character (52), the ^{207}Pb NMR data on $M@Pb_{12}^{2-}$ ions is the only confirmation of such effects. (The NMR properties for $M@Sn_{12}^{2-}$ are not known.) Moreover, solution-phase syntheses have provided crystalline examples of many of these clusters, such as Pb_{10}^{2-}, $M@Pb_{12}^{2-}$ (M = Ni, Pd, Pt), $Ir@Sn_{12}^{3-}$, and $Ni@Pb_{10}^{2-}$ (44, 46, 53). Further, mass spectrometric studies showed that empty cage E_{10}^{2-} and E_{12}^{2-} clusters and their $M@E_{12}^{2-}$ endohedral derivatives are particularly stable among their stoichiometric neighbors (6, 44, 45). Among gaseous ionic clusters, Wang's extensive photoelectron spectroscopic studies on anionic endohedral $M@Sn_n$ complexes (54–57) complement Lievens discovery of stable metal-encapsulated $Al@Pb_{10}^{+}$ and $Al@Pb_{12}^{+}$ cluster cations through molecular beam/mass spectrometry experiments and complementary density functional theory (DFT) calculations (58).

Herein, we report anion photoelectron spectroscopic (PES) and computational results of the geometries and electronic structures of $Pt@Pb_{10}^{1-}$ and $Pt@Pb_{12}^{1-/2-}$ clusters. Magnetic susceptibility measurements were also conducted on crystalline $[K(2,2,2\text{-crypt})]_2[Pt@Pb_{12}]$. Through the combined use of synthesis, photoelectron spectroscopy and DFT, we directly compare electronic and geometric structures of gas-phase clusters with those known in the solid state. We demonstrate that the endohedral $M@Pb_{12}^{n-}$ and $M@Pb_{10}^{n-}$ clusters represent the only other example of bare clusters outside of the fullerene family that have been characterized in the gas phase, in solution, and in the solid state. Specifically and in analogy to C_{60}, the $Pt@Pb_{12}^{2-}$ maintains its electronically degenerate icosahedral geometric structure in all three phases and exhibits enhanced stability relative to the other compositional members of its class. Interestingly, C_{60} was first discovered in the gas phase and later synthesized in bulk, whereas the endohedral $M@Pb_{12}^{n-}$ and $M@Pb_{10}^{n-}$ clusters were initially discovered through synthesis of crystalline samples and then vaporized into the gas phase where they were structurally characterized through the synergetic combination of anion photoelectron spectroscopy and DFT computations (this study).

Author contributions: M.R.P., K.H.B., and B.W.E. designed research; A.G., H.W., X.L., Y.-J.K., F.S.K., M.R.P., K.H.B., and B.W.E. performed research; A.G., H.W., Y.-J.K., F.S.K., M.R.P., K.H.B., and B.W.E. analyzed data; and A.G., X.L., M.R.P., K.H.B., and B.W.E. wrote the paper.

The authors declare no conflict of interest.

This article is a PNAS Direct Submission.

[1]To whom correspondence may be addressed. E-mail: kbowen@jhu.edu, eichhorn@umd.edu, or pederson@dave.nrl.navy.mil.

This article contains supporting information online at www.pnas.org/lookup/suppl/doi:10.1073/pnas.1105052108/-/DCSupplemental.

Experimental

Synthesis. Modifications of previous methods were used to synthesize the $Pt@Pb_{12}^{2-}$ samples (44, 46). Melts of nominal composition K_4Pb_9 were made by fusion of stoichiometric ratios of the elements at high temperature, sealed in evacuated silica tubes, and heated carefully with a natural gas/oxygen flame. (Caution! Molten alloy synthesis can result in serious explosions, and reactions should be conducted with great caution behind blast shields.) The 4,7,13,16,21,24-hexaoxa-1,10-diazobicyclo[8,8,8]-hexacosane (2,2,2-crypt) was purchased from Aldrich. $Pt(PPh_3)_4$ were purchased from Strem. Anhydrous ethylenediamine (EN) was purchased from Fisher, vacuum distilled from K_4Sn_9, and stored under dinitrogen. Toluene was distilled from sodium/benzophenone under dinitrogen and stored under dinitrogen. Syntheses were performed in a nitrogen atmosphere dry box. In vial 1, K_4Pb_9 (80 mg, 0.039 mmol) and 2,2,2-crypt (59.6 mg, 0.156 mmol) were dissolved in EN (2 mL) and stirred for 5 min, yielding a dark-green solution. In vial 2, $Pt(PPh_3)_4$ (49 mg, 0.039 mmol) was dissolved in toluene (1 mL) yielding a pale-yellow solution. The solution from vial 2 was added dropwise to vial 1, and the mixture was stirred for 2 h, yielding a reddish-brown solution. The solution was then filtered through packed glass wool. After 2 d, red-black crystals of $Pt@Pb_{12}^{2-}$ formed in the reaction vessel. The crystalline yield was approximately 50 mg (60%).

Photoelectron Spectroscopy. Anion photoelectron spectroscopy was conducted by crossing a beam of mass-selected negative ions with a fixed-frequency photon beam and energy analyzing the resultant photodetached electrons. The photodetachment process is governed by the energy-conserving relationship, $h\nu = \text{EBE} + \text{EKE}$, where $h\nu$ is the photon energy, EBE is the electron binding energy, and EKE is the electron kinetic energy. Details of our apparatus have been described elsewhere (59). Briefly, the apparatus consists of an ion source, a linear TOF mass selector, a neodymium-doped yttrium/aluminum-garnet (Nd:YAG) photodetachment laser, and a magnetic bottle (MB) photoelectron spectrometer. The instrumental resolution of our MB photoelectron spectrometer is approximately 35 meV at EKE = 1 eV. The fourth harmonic (266 nm, 4.661 eV) of a Nd:YAG laser was used to photodetach the cluster anions of interest. Photoelectron spectra were calibrated against the known atomic lines of Cu^-.

To introduce the sample into the gas phase, a specialized source was employed that combined pulsed infrared desorption to bring neutral sample molecules into the gas phase, pulsed photoemission to provide low-energy electrons for attachment, and a pulsed helium jet expansion for cooling and transport of the resultant anions. This infrared desorption/photoemission (IR/PE) source has been previously described in detail (60). Briefly, a short IR pulse (1,064 nm) from a Nd:YAG laser hits a translating graphite bar thinly coated with sample. Because the graphite absorbed most of the energy, a localized thermal shock incident upon the surface propels mostly intact sample material into the gas phase. An almost simultaneous pulse of 532-nm light from a second Nd:YAG laser strikes a photoemitter (Y_2O_3 disk) creating a shower of low-energy electrons that attach to the evaporated neutral species. A plume of ultrahigh purity (UHP) helium gas expanded from a pulsed valve located upstream cools the nascent plasma mixture and guides it into the mass spectrometer, where it is analyzed.

Due to the sample's air sensitivity, the graphite bar was enclosed inside an airtight container and only opened under high vacuum. The crystalline $[K(2,2,2\text{-crypt})]_2[Pt@Pb_{12}]$ sample was burnished onto the rod and sealed in the airtight container inside a glove box, which maintained an oxygen-free nitrogen atmosphere. The generation of pure lead cluster anions was accomplished with a laser vaporization source (31). There, a 532-nm laser pulse struck a rotating, translating high-purity lead rod. The evaporated material was entrained into a plume of UHP helium gas and guided through a condensation channel, where it cooled, condensed, and formed clusters.

Magnetic Susceptibility. Magnetic measurements were recorded from 5 to 293 K with a Quantum Design superconducting quantum interference device magnetometer. A crystalline sample of $[K(2,2,2\text{-crypt})]_2[Pt@Pb_{12}]$ was loaded into a gelatin capsule in a dry box and anaerobically transferred to the magnetometer in a He purge.

Theoretical

The Gaussian-orbital-based calculations and geometry optimizations presented here were performed using the NRLMOL suite of density functional codes (61–65). Many starting geometries with different symmetries were fully relaxed, and those exhibiting relatively low energies were saved for additional analysis. For most of the 13-atom clusters, Jahn–Teller effects induced slight distortions from icosahedral symmetry. As shown in Table 1, low-energy structures for the 11-atom clusters were found with D_{5d}, D_{5h}, D_{4d}, and D_{4h} symmetry and exhibited varying degrees of stability. For all charge states, the D_{4d} structure was found to be the most stable and the monocharged anion was found to be the most stable. For each low-energy structure and charge state, the vertical photoemission (anion photoelectron) spectra were calculated. Comparison of simulated and experimental spectra aided in ascertaining the most probable ground-state geometries. The methods used here have been described previously (66).

Results

A typical anion mass spectrum of $[K(2,2,2\text{-crypt})]_2[Pt@Pb_{12}]$ obtained by employing the IR/PE source for introducing the sample into gas phase is shown in Fig. 1. Despite the use of pure salts containing preformed $Pt@Pb_{12}^{2-}$ clusters for the source, the spectrum contains four major series of ions; namely, Pb_n^- ($n = 6$–10), $PtPb_n^-$ ($n = 6$–12), and the potassium ion pairs KPb_n^- ($n = 8$–10) and $KPtPb_n^-$ ($n = 10$–12). The bare Pb_n^- clusters and their potassium salts, KPb_n^-, appear primarily at low n values. Above $n = 10$, $PtPb_n^-$ and $KPtPb_n^-$ clusters are the main species observed, with $PtPb_n^-$ species dominating. A transition occurs at $n = 10$ and appears remarkably well defined; few Pb_n^- clusters are observed for $n > 10$ and a reduced contribution from the $PtPb_n^-$ series is present among sizes, $n < 10$. The strongest peaks among the $PtPb_n^-$ series correspond to $PtPb_{10}^-$ [2,268 atomic mass units (amu)] and $PtPb_{12}^-$ (2,682 amu), and the $PtPb_n^-$ series abruptly ends at $n = 12$. These findings are consistent with the solution-phase studies (44) that showed forma-

Table 1. Relative energies of the $Pt@Pb_{10}^{n-}$ clusters

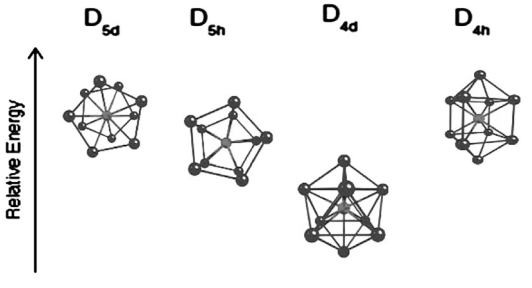

Excess energy (eV) in $Pt@Pb_{10}^{n-}$ clusters

n	D_{5d}	D_{5h}	D_{4d}	D_{4h}
0	4.97	4.42	3.08	5.16
1	1.66	1.39	0.00	2.11
2	1.53	1.27	0.32	2.13
3	4.05	4.16	2.73	5.14

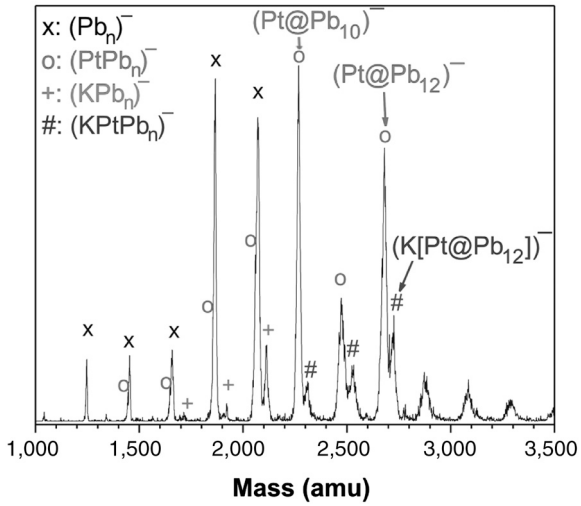

Fig. 1. Anion mass spectrum of $[K(2,2,2\text{-crypt})]_2[Pt@Pb_{12}]$ sample obtained by employing our IR/PE anion source.

tion of only two Pt-Pb clusters: $Pt@Pb_{12}^{2-}$ and $Pt@Pb_{10}^{2-}$. The $Pt@Pb_{12}^{2-}$ ion has been crystallographically characterized (44), however, only the $Ni@Pb_{10}^{2-}$ nickel analog of $Pt@Pb_{10}^{2-}$ has been characterized in the solid state. Importantly, the photoelectron spectra of $PtPb_{10}^-$ (2,268 amu) and $PtPb_{12}^-$ (2,682 amu) look quite different from potentially mass-coincident Pb_{11}^- (2,280 amu) and Pb_{13}^- (2,695 amu) cluster anions (67), respectively, thus supporting our mass spectral assignment.

The small satellite peaks at approximately 40-amu-higher mass next to the Pb_n^- and $PtPb_n^-$ series belong to potassium-containing series KPb_n^- and $KPtPb_n^-$, respectively. The presence of such ions provides access to doubly charged cluster anions. The peaks above 2,700 amu in Fig. 1 belong to a fifth series of ions, $Pt_2Pb_n^-$, where $n = 12$–16. These structures are presumably related to the "two-focus" endohedral clusters known for tin, such as the $Pt_2Sn_{17}^{4-}$ and $Pd_2Sn_{18}^{4-}$ anions (6, 41). Mass spectral simulations of these data (Figs. S1 and S2) confirm their identity and show that multifocus clusters of lead are also accessible but appear to have different nuclearities and structures than the multifocus Sn series. Similar fragmentation and gas-phase cluster growth processes were observed in the laser desorption/ionization MS studies of $[K(2,2,2\text{-crypt})]_4[Pd_2Sn_{18}]$ crystals and, to a lesser extent, the electrospray ionization MS studies of $[K(2,2,2\text{-crypt})]_2[PtSn_9Pt(PPh_3)]$. Although there is a rich series of new Pt-Pb cluster ions evident in Fig. 1, our PES studies below focus on the $PtPb_{10}^-$ and $PtPb_{12}^-$ clusters of the primary series.

The photoelectron spectra of $PtPb_{10}^-$ and $PtPb_{12}^-$ are shown in Fig. 2 along with the spectra of the pure (empty cage) parent clusters, Pb_{10}^- and Pb_{12}^-. The photoelectron spectra of both Pb_{10}^- and Pb_{12}^- had been recorded previously (68). In both the lead 10 and 12 series, the PE data for the filled and empty clusters are similar in regard to both their electron binding energies and their complexities, suggesting that their electronic structures are primarily lead based.

The spectrum of $PtPb_{10}^-$ is relatively complicated and displays at least six resolved transitions—i.e., EBE $= 2.80 \pm 0.05$, 3.10 ± 0.05, 3.45 ± 0.05, 3.60 ± 0.05, 4.0 ± 0.1, 4.40 ± 0.05 eV. The onset of photoelectron intensity occurs at 2.7 ± 0.1 eV. Based on the known structures of related clusters, several geometrical symmetries seemed plausible. For example, two different geometries have been identified for $M@E_{10}^{n-}$ clusters; namely, D_{4d} (M = Ni; E = Pb; $n = 2$) and D_{5h} (M = Co, Fe; E = Ge; $n = 3$) (69, 70). Table 1 shows the optimized geometries (NRLMOL) for the four most viable structures for the $PtPb_{10}^{n-}$ ions where $n = 0$, 1, 2, 3. Their energies relative to the lowest-energy structure, D_{4d} $PtPb_{10}^-$ are given in electron volts in Table 1, and the calculated anion photoelectron spectra for all four symmetries of the $PtPb_{10}^-$ cluster appear in Fig. 3. The D_{4d} structure has the lowest energy for each charge state $n = 0$, 1, 2, and 3 (see Table 1), which is consistent with the observed solid-state structure of $Ni@Pb_{10}^{2-}$. The D_{5h} geometry is the next closest energy structure for the $n = 0$, 1, and 2 charge states, and is 0.95–1.39-eV higher in energy relative to the D_{4d} structure. In the case of $n = 3$, the D_{5d} structure is slightly lower in energy (0.11 eV) relative to the D_{5h} structure, but both are more than 1.3-eV higher in energy relative to the D_{4d} structure. In all cases, the D_{4h} bicapped square antiprism is the least stable structure.

Both the D_{4h} and D_{4d} structures give calculated photoelectron spectral patterns (Fig. 3) consistent with the observed photoelectron spectra for the $PtPb_{10}^-$ ion (Fig. 2), whereas the D_{5h} and D_{5d} calculated spectra are quite different. Because the D_{4d} structure observed in the solid state (44, 45) has the lowest calculated energy of the four optimized geometries and gives a reasonable match to the experimental photoelectron data, we believe this geometry is adopted by the $PtPb_{10}^-$ cluster in the gas phase. The superposition of the calculated and observed PES data is shown in Fig. 2.

The PE spectrum of $PtPb_{12}^-$ displays four prominent transitions—i.e., EBE $= 3.1 \pm 0.1$, 3.25 ± 0.05, 3.75 ± 0.05, 4.05 ± 0.05 eV. The onset of photoelectron intensity in the spectrum of $PtPb_{12}^-$ occurs at 2.8 ± 0.1 eV. The small feature with a maximum at 2.7 eV originates from a contaminant—most likely the mass-coincident Pb_{13}^- ion. The simulated PE spectrum of $PtPb_{12}^-$ is overlaid on the experimental PE spectrum presented in Fig. 2.

The photoelectron spectra of Pb_{12}^-, $PtPb_{12}^-$, and $KPtPb_{12}^-$ presented in Fig. 4 are in excellent agreement with the calculated spectra for $PtPb_{12}^-$ (see Fig. 2). The PE spectrum of $KPtPb_{12}^-$ exhibits three prominent transitions at EBE $= 2.8 \pm 0.1$, 3.4 ± 0.1, and 3.6 ± 0.1 eV. The onset of photoelectron intensity occurs at 2.4 ± 0.1 eV. Because $PtPb_{12}^{2-}$ is known from both solid-state and computational studies to be a highly stable anion, $KPtPb_{12}^-$ is best characterized as $K^+[PtPb_{12}^{2-}]$. Thus, the study of $KPtPb_{12}^-$ offers a glimpse into the electronic properties of the endohedral $Pt@Pb_{12}^{2-}$ dianion and the effect of its ion pairing. The data suggest that Pb_{12}^-, $PtPb_{12}^-$, and $PtPb_{12}^{2-}$ all exist as nearly regular icosahedra with little change in electronic or atomic structure due to oxidation or insertion of a transition metal into the cluster core.

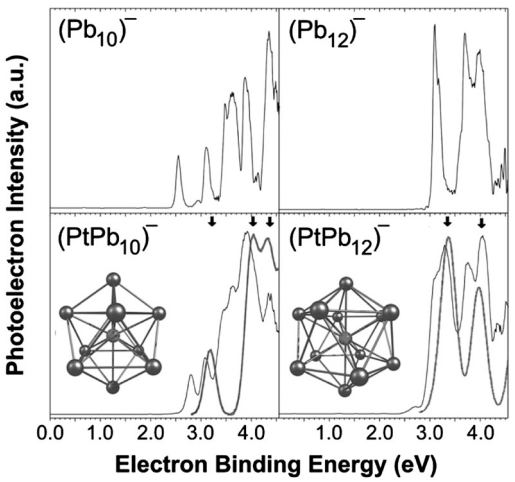

Fig. 2. Photoelectron spectra of $PtPb_{10}^-$ and $PtPb_{12}^-$ (*Lower*) as well as Pb_{10}^- and Pb_{12}^- (*Upper*) recorded with 266-nm photons. The calculated structures of the Pt-containing clusters along with the predicted photoelectron transitions (arrows) are also shown. Simulated photoelectron spectra (dark lines) are obtained by convolving the predicted transitions with Gaussians whose widths correspond to experimental resolution.

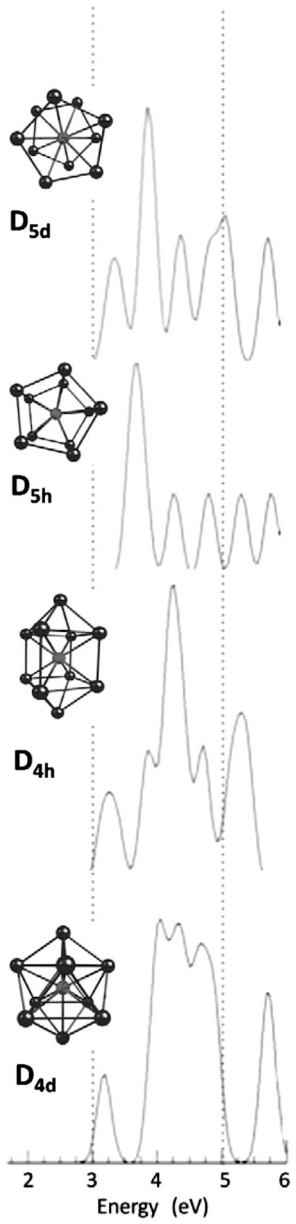

Fig. 3. Calculated photoelectron spectra for the $PtPb_{10}^-$ in four different structures: eclipsed pentagonal prism (D_{5h}), staggered pentagonal prism (D_{5d}), bicapped square prism (D_{4h}), and bicapped square antiprism (D_{4d}). The spectra were calculated from differences in total energy. The dotted lines are a guide to the eye.

The simplicity of both $PtPb_{12}^-$ and $KPtPb_{12}^-$ PE spectra is further consistent with their high orbital degeneracies and density of states near the highest-occupied molecular orbital (HOMO). The similarity of these spectra also suggests that ion pair formation between K^+ and $PtPb_{12}^{2-}$ does not significantly affect the cluster moiety. The only difference is a systematic shift of the observed transitions to approximately 0.4-eV-lower values relative to the monoanion. Similar shifts are known to occur upon introduction of alkali atoms in related clusters (27, 68, 71).

The high orbital degeneracy in the $Pt@Pb_{12}^{2-}$ cluster has been shown to give rise to aromatic behavior and unusual NMR chemical shifts. To probe for anomalous effects due to circulating electrons, such as a temperature-independent paramagnetic moment similar to a metal, we evaluated the magnetic susceptibility of the $[K(2,2,2\text{-crypt})]_2[Pt@Pb_{12}]$ complex down to 5 K. The data showed typical diamagnetic behavior down to 7 K, with a weak

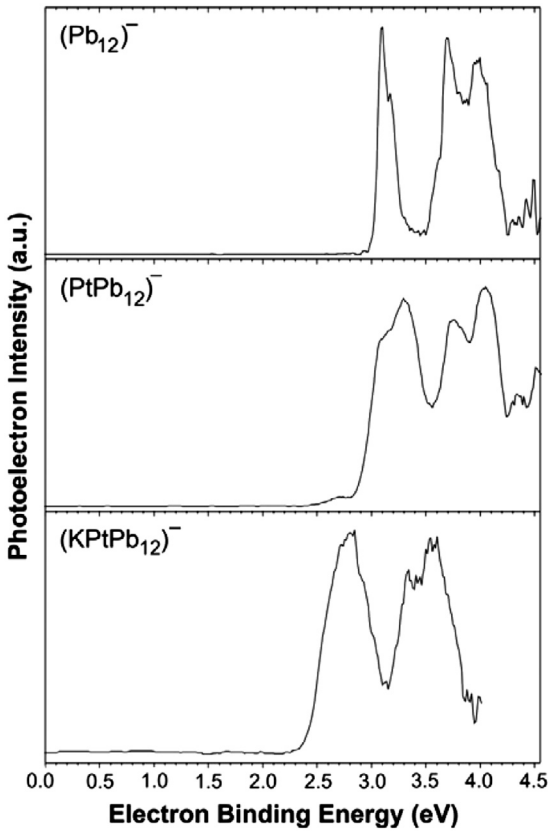

Fig. 4. Photoelectron spectra of Pb_{12}^- (*Top*), $PtPb_{12}^-$ (*Middle*), and $KPtPb_{12}^-$ (*Bottom*) recorded with 266-nm photons.

superconducting transition below 7 K due to a trace metallic Pb impurity (Fig. S3).

Discussion

It is well known that the energy differences between competing geometries of deltahedral Zintl clusters can be exceedingly small (72–75). In solution, insertion of endohedral metal atoms can stabilize one structure over another in isoelectronic clusters, such as the formation of the D_{3h} $Cu@Sn_9^{3-}$ from the C_{4v} Sn_9^{4-} parent through the insertion of Cu^+. Whether these changes are due to crystal packing forces, small electronic changes, or solvation effects is very difficult to ascertain from typical crystallographic and solution NMR studies because of the high symmetries and high fluxionalities of clusters (73). Furthermore, the relationship between gas-phase structures and those observed in the solid state are virtually unknown because of the differences in charge states (gas-phase ions are typically −1, whereas ions in solution have charges of −2 or greater). Through the use of preformed cluster precursors, mass spectrometry, photoelectron spectroscopy, and DFT modeling, we help bridge this gap by showing that Pb_{12}^-, $PtPb_{12}^-$, and $KPtPb_{12}^-$ (i.e., $K^+[PtPb_{12}^{2-}]$) maintain the same structures in the gaseous and the condensed phases.

Comparison of the photoelectron transitions of $PtPb_{10}^-$ and Pb_{10}^- show that electron binding to the Pb_{10}^- cluster is approximately 0.2-eV stronger when the Pt atom is inserted. Moreover, the similarity in appearance of the photoelectron spectra of the two ions (Fig. 2) suggests similar electronic structures. The DFT calculations show that $PtPb_{10}^-$ and Pb_{10}^- as well as $PtPb_{10}^{2-}$ and Pb_{10}^{2-} adopt the square antiprismatic D_{4d} structures experimentally observed in the crystal structures of the dianions. The similarity in structure is also in accord with a Wade–Mingos analysis. For example, the Sn_9^{4-} and $Cu@Sn_9^{3-}$ ions are both formally *nido* $2n + 4$ clusters (i.e., the same structural class) but have C_{4v} and D_{3h} structures, respectively. The persistence of this D_{4d} struc-

ture for the $Pb_{10}^{1-/2-}$ clusters in the condensed state is somewhat surprising in view of the highly dynamic nature of the $M@Pb_{10}^{2-}$ structures in solution (i.e., there are two or more structures very close in energy) and the existence of alternate structures in the closely related germanides (69, 70).

In contrast to the Pb_{10} clusters, the photoelectron spectra for the $PtPb_{12}^-$ and Pb_{12}^- ions exhibit fewer features and, with the exception of broader transitions for the case of $PtPb_{12}^-$, are strikingly similar. These data suggest that the HOMOs of each are highly degenerate lead-based states that are not significantly affected by the interstitial Pt atom. Although the high degree of orbital degeneracy is clearly evident from the PES data, DFT calculations, and NMR spectroscopic studies, the apparent σ-aromaticity does not induce a noticeable temperature-independent paramagnetism that might have been anticipated from such ring currents.

The similarity between the PE spectra of $PtPb_{12}^-$ and $KPtPb_{12}^-$ (i.e., $K^+[PtPb_{12}^{2-}]$) also suggests that the structure of $PtPb_{12}^{2-}$ is retained in the $PtPb_{12}^-$ monoanion. The PE data for the $PtPb_{12}^{2-}$ species is indicative of highly degenerate electronic states consistent with its theoretically predicted and experimentally observed slightly distorted I_h symmetry. The robust nature of these photoelectron properties is attributed to the stability of the Pb_{12}^{2-} icosahedral structure.

In summary, the combined gas-phase, solution-phase, and solid-state investigations suggest that D_{4d} $Pt@Pb_{10}^{1-}$ and I_h $Pt@Pb_{12}^{2-/1-}$ species are stable entities in all three states. This observation is in contrast to related $M@Al_{12}^{1-}$ (M = Al, B), $Al@Pb_{12}^+$, and other $M@E_{12}^{n-}$ gas-phase clusters that are not known in the condensed phase. Moreover, it is not clear if they exist outside of ultrahigh vacuum conditions. Although gas-phase studies of Al_{13}^- show that it is uniquely stable among the Al_n^- series, the Pb_n^- clusters and their endohedral cousins, the $Pt@Pb_n^-$ clusters, show two species with enhanced stability—one at $n = 10$ and another at $n = 12$. However, the electronic stability of the icosahedral $n = 12$ clusters, as evidenced by the NMR and PES properties, seems to be superior to the $n = 10$ series, likely because of the enhanced aromaticity of the icosahedron. In addition, the mass spectroscopic studies show higher order, dual focus clusters such as $Pt_2Pb_n^-$ where $n = 12$–16. These ions represent a class of endohedral clusters that are structurally distinct from the species, $M_2@E_{17}^{4-}$ and $M_2@E_{18}^{4-}$, known in the condensed phase for M = Ni, Pd, Pt, and E = Ge, Sn (41,76–78).

ACKNOWLEDGMENTS. Work was supported by the Division of Materials Science and Engineering, Basic Energy Sciences, US Department of Energy, under Grant DE-FG02-09ER46558 (to K.H.B.) and by the National Science Foundation under Grant 0944528 (to B.W.E.). Computational work (M.R.P.) was partially supported by the Naval Research Laboratory and the High Performance Computing Modernization Office program.

1. Joannis A (1891) Action of sodammonium and potassammonium on metals. *C R Hebd Seances Acad Sci* 113:795–798.
2. Sevov SC, Goicoechea JM (2006) Chemistry of deltahedral zintl ions. *Organometallics* 25:5678–5692.
3. Fässler TF, Hoffmann SD (2004) Endohedral zintl ions: Intermetalloid clusters. *Angew Chem Int Ed Engl* 43:6242–6247.
4. Fässler TF (2001) The renaissance of homoatomic nine-atom polyhedra of the heavier carbon-group elements Si-Pb. *Coord Chem Rev* 215:347–377.
5. Corbett JD (2000) Polyanionic clusters and networks of the early p-element metals in the solid state: Beyond the zintl boundary. *Angew Chem Int Ed Engl* 39:670–690.
6. Scharfe S, Kraus F, Stegmaier S, Schier A, Fässler TF (2011) Zintl ions, cage compounds, and intermetalloid clusters of group 14 and group 15 elements. *Angew Chem Int Ed Engl* 50:3630–3671.
7. Corbett JD (1985) Polyatomic zintl anions of the post-transition elements. *Chem Rev* 85:383–397.
8. Haushalter RC, O'Connor CJ, Umarji AM, Shenoy GK, Saw CK (1984) Spin glass behavior in the new amorphous alloys M_2SnTe_4 (M = Cr, Mn, Fe). *Solid State Comm* 49:929–933.
9. Haushalter RC, O'Connor CM, Haushalter JP, Umarji AM, Shenoy GK (1984) Synthesis of new amorphous metallic spin glasses M_2SnTe_4 (M = Cr, Mn, Fe, Co): Solvent induced metal-insulator transformations. *Angew Chem Int Ed Engl* 23:169–170.
10. Treacy MMJ, Haushalter RC, Rice SB (1987) Transmission electron microscopy study of the reaction of Sn_{4-9} zintl ions with single crystal Au films. *Ultramicroscopy* 23:135–149.
11. O'Connor CJ, Foise JW, Haushalter RC (1987) Spin glass behavior in some ternary metal chalcogens. *Proc Indian Acad Sci Chem Sci* 98:69–78.
12. Haushalter RC, Goshorn DP, Sewchok MG, Roxlo CB (1987) Chemical control of the electronic properties in the amorphous alloys M_2SnTe_4 (M = Mn, Fe, Co, Cu). *Mater Res Bull* 22:761–768.
13. Foise JW, O'Connor CJ, Haushalter RC (1987) Unusual magnetic behavior of the amorphous metallic materials M_2SnTe_4 where M = Co and Ni. *Solid State Comm* 63:349–351.
14. Boeddinghaus MB, Hoffmann SD, Fassler TF (2007) Synthesis and crystal structure of $[K([2.2]crypt)]_2[HgGe_9](dmf)$. *Z Anorg Allg Chem* 633:2338–2341.
15. Ugrinov A, Sevov SC (2003) $[Ge_9 = Ge_9 = Ge_9 = Ge_9]^{8-}$: A linear tetramer of nine-atom germanium clusters, a nanorod. *Inorg Chem* 42:5789–5791.
16. Hauptmann R, Fässler TF (2003) Low dimensional arrangements of the zintl ion $[Ge_9\text{-}Ge_9]^{6-}$ and chemical bonding in $[Ge^6]^{2-}$, $[Ge_9\text{-}Ge_9]^{6-}$, and $\infty 1\{[Ge_9]\}^{2-}$. *Z Anorg Allg Chem* 629:2266–2273.
17. Kesanli B, Fettinger J, Eichhorn B (2003) Controlled aggregation of ME_8^{n-} binary anions (M = Cr, Mo; E = As, Sb) into one-dimensional arrays: Structures, magnetism and spectroscopy. *J Am Chem Soc* 125:7367–7376.
18. Kesanli B, Fettinger J, Scott B, Eichhorn B (2004) Gas phase, solution, and solid state alkali ion binding by the $[NbE_8]^{3-}$ (E = As, Sb) complexes: Synthesis, structure, and spectroscopy. *Inorg Chem* 43:3840–3846.
19. Downie C, Tang Z, Guloy AM (2000) An unprecedented $1/\infty[Ge_9]^{2-}$ polymer: A link between molecular zintl clusters and solid-state phases. *Angew Chem Int Ed Engl* 39:337–340.
20. Nienhaus A, Hauptmann R, Fässler TF (2002) $1/\infty[HgGe_9]^{2-}$—A polymer with zintl ions as building blocks covalently linked by heteroatoms. *Angew Chem Int Ed Engl* 41:3213–3215.
21. Sun D, et al. (2006) Hexagonal nanoporous germanium through surfactant-driven self-assembly of Zintl clusters. *Nature* 441:1126–1130.
22. Guloy AM, et al. (2006) A guest-free germanium clathrate. *Nature* 443:320–323.
23. Armatas GS, Kanatzidis MG (2008) High-surface-area mesoporous germanium from oxidative polymerization of the deltahedral $[Ge_9]^{4-}$ cluster: Electronic structure modulation with donor and acceptor molecules. *Adv Mater* 20:546–550.
24. Fässler TF (2001) Homoatomic polyhedra as structural modules in chemistry: What binds fullerenes and homonuclear zintl ions? *Angew Chem Int Ed Engl* 40:4161–4165.
25. Tanke RS, et al. (2003) Synthesis of germanium nanoclusters with irreversibly attached functional groups: Acetals, alcohols, esters, and polymers. *Chem Mater* 15:1682–1689.
26. Mayeri D, Phillips BL, Augustine MP, Kauzlarich SM (2001) NMR study of the synthesis of alkyl-terminated silicon nanoparticles from the reaction of $SiCl_4$ with the zintl salt, NaSi. *Chem Mater* 13:765–770.
27. Zheng WJ, Thomas OC, Lippa TP, Xu SJ, Bowen KH (2006) The ionic KAl_{13} molecule: A stepping stone to cluster-assembled materials. *J Chem Phys* 124:144304–144305.
28. Perez A, et al. (1997) Cluster assembled materials: A novel class of nanostructured solids with original structures and properties. *J Phys D Appl Phys* 30:709–721.
29. Jena P, Khanna SN, Rao BK (1996) *Cluster Assembled Materials.* (Trans Tech Publ, Zurich), 232, pp 1–25.
30. Castleman AW, Bowen KH (1996) Clusters: Structure, energetics, and dynamics of intermediate states of matter. *J Phys Chem* 100:12911–12944.
31. Kroto HW, Heath JR, O'Brien SC, Curl RF, Smalley RE (1985) C60: Buckminsterfullerene. *Nature* 318:162–163.
32. Kratachmer W, Lamb LD, Fostiropoulos K, Huffman DR (1990) Solid C_{60}: A new form of carbon. *Nature* 347:354–358.
33. Guo BC, Kerns KP, Castleman AW (1992) $Ti_8C_{12}^+$-metallo-carbohedrenes: A new class of molecular clusters? *Science* 255:1411–1413.
34. Wei S, Guo BC, Purnell J, Buzza S, Castleman AW (1992) Metallo-carbohedrenes: Formation of multicage structures. *Science* 256:818–820.
35. Leskiw BD, Castleman AW (2000) The interplay between the electronic structure and reactivity of aluminum clusters: Model systems as building blocks for cluster assembled materials. *Chem Phys Lett* 316:31–36.
36. Li X, Wu H, Wang X-B, Wang L-S (1998) s-p Hybridization and electron shell structures in aluminum clusters: A photoelectron spectroscopy study. *Phys Rev Lett* 81:1909–1912.
37. Goicoechea JM, Sevov SC (2006) Organozinc derivatives of deltahedral zintl ions: Synthesis and characterization of closo-$[E_9Zn(C_6H_5)]^{3-}$ (E = Si, Ge, Sn, Pb). *Organometallics* 25:4530–4536.
38. Goicoechea JM, Sevov SC (2005) $[(Pd\text{-}Pd)@Ge_{18}]^{4-}$: A palladium dimer inside the largest single-cage deltahedron. *J Am Chem Soc* 127:7676–7677.
39. Goicoechea JM, Sevov SC (2005) $[(Ni\text{-}Ni\text{-}Ni)@(Ge_9)_2]^{4-}$: A linear triatomic nickel filament enclosed in a dimer of nine-atom germanium clusters. *Angew Chem Int Ed Engl* 44:4026–4028.
40. Scharfe S, Fässler TF, Stegmaier S, Hoffmann SD, Ruhland K (2008) $[Cu@Sn_9]^{3-}$ and $[Cu@Pb_9]^{3-}$: Intermetalloid clusters with endohedral Cu atoms in spherical environments. *Chem Eur J* 14:4479–4483.
41. Sun Z-M, Xiao H, Li J, Wang L-S (2007) $Pd_2@Sn_{18}^{4-}$: Fusion of two endohedral stannaspherenes. *J Am Chem Soc* 129:9560–9561.
42. Lips F, Clerac R, Dehnen S (2011) $[Eu@Sn_6Bi_8](4-)$: A mini-fullerane-type Zintl anion containing a lanthanide ion. *Angew Chem Int Ed Engl* 50:955–959.

43. Lips F, Clerac R, Dehnen S (2011) Neither electron-precise nor in accordance with Wade-Mingos rules: The ternary cluster anion $[Ni_2Sn_7Bi_5](3-)$. *Angew Chem Int Ed Engl* 50:960–964.
44. Esenturk EN, Fettinger JC, Eichhorn BW (2006) The Pb_{12}^{2-} and Pb_{10}^{2-} Zintl ions and the $M@Pb_{12}^{2-}$ and $M@Pb_{10}^{2-}$ cluster series where M = Ni, Pd, Pt. *J Am Chem Soc* 128:9178–9186.
45. Esenturk EN, Fettinger JC, Eichhorn BW (2005) The closo-Pb_{10}^{2-} Zintl ion in the $[Ni@Pb_{10}]^{2-}$ cluster. *Chem Commun* 2005:247–249.
46. Esenturk EN, Fettinger JC, Lam YF, Eichhorn BW (2004) $Pt@Pb_{12}^{2-}$. *Angew Chem Int Ed Engl* 43:2132–2134.
47. Moses MJ, Fettinger JC, Eichhorn BW (2003) Interpenetrating As_{20} fullerene and Ni_{12} icosahedra in the onion-skin $[As@Ni_{12}@As_{20}]^{3-}$ ion. *Science* 300:778–780.
48. Kesanli B, Fettinger JC, Gardner DR, Eichhorn BJ (2002) The $[Sn_9Pt_2(PPh_3)]^{2-}$ and $[Sn_9Ni_2(CO)]^{3-}$ complexes: Two markedly different Sn_9M_2 L transition metal zintl ion clusters and their dynamic behavior. *J Am Chem Soc* 124:4779–4786.
49. Fässler TF, Hoffmann S (1999) Valence compounds at the border to intermetallics: Alkali and alkaline earth metal stannides and plumbides. *Z Kristallogr* 214:722–734.
50. Moses MJ, Fettinger JC, Eichhorn BW (2007) The $[Ni_5Sb_{17}]^{4-}$ transition metal zintl ion complex: Crossing the zintl border in molecular intermetalloid clusters. *Inorg Chem* 46:1036–1038.
51. Goicoechea JM, Sevov SC (2006) $[Zn_9Bi_{11}]^{5-}$: A ligand-free intermetalloid cluster. *Angew Chem Int Ed Engl* 45:5147–5150.
52. Chen ZF, King RB (2005) Spherical aromaticity: Recent work on fullerenes, polyhedral boranes, and related structures. *Chem Rev* 105:3613–3642.
53. Spiekermann A, Hoffinann SD, Fassler TF (2006) The zintl ion $[Pb_{10}]^{2-}$: a rare example of a homoatomic closo-cluster. *Angew Chem Int Ed Engl* 45:3459–3462.
54. Wang LS, Cui LF (2008) Stable icosahedral hollow cage clusters: Stannaspherene (Sn_{12}^{2-}) and plumbaspherene (Pb_{12}^{2-}). *Int Rev Phys Chem* 27:139–166.
55. Cui LF, Huang X, Wang LM, Li J, Wang LS (2006) Pb_{12}^{2-}: Plumbaspherene. *J Phys Chem A* 110:10169–10172.
56. Wang LS, et al. (2006) Sn_{12}^{2-}: Stannaspherene. *J Am Chem Soc* 128:8390–8391.
57. Cui LF, Huang X, Wang LM, Li J, Wang LS (2007) Endohedral stannaspherenes ($M@Sn_{12}^{-}$): A rich class of stable molecular cage clusters. *Angew Chem Int Ed Engl* 46:742–745.
58. Neukermans S, et al. (2004) Extremely stable metal-encapsulated $AlPb_{10}^{+}$ and $AlPb_{12}^{+}$ clusters: Mass-spectrometric discovery and density functional theory study. *Phys Rev Lett* 92:163401.1–163401.4.
59. Gerhards M, Thomas OC, Nilles JM, Zheng WJ, Bowen KH (2002) Cobalt—benzene cluster anions: Mass spectrometry and negative ion photoelectron spectroscopy. *J Chem Phys* 116:10247–10252.
60. Stokes ST, Li X, Grubisic A, Ko YJ, Bowen KH (2007) Intrinsic electrophilic properties of nucleosides: Photoelectron spectroscopy of their parent anions. *J Chem Phys* 127:084321–084326.
61. Pederson MR, Porezag DV, Kortus J, Patton DC (2000) Strategies for massively parallel local-orbital-based electronic structure methods. *Phys Status Solidi B* 217:197–218.
62. Liu AY, Quong AA (1996) Linear-response calculation of electron-phonon coupling parameters. *Phys Rev B* 53:R7575–R7579.
63. Porezag D, Pederson MR, Liu AY (1999) Importance of nonlinear core corrections for density-functional based pseudopotential calculations. *Phys Rev B* 60:14132–14139.
64. Porezag D, Pederson MR (1999) Optimization of Gaussian basis sets for density-functional calculations. *Phys Rev A* 60:2840–2847.
65. Perdew JP, Burke K, Ernzerhof M (1996) Generalized gradient approximation made simple. *Phys Rev Lett* 77:3865–3868.
66. Ashman C, Khanna SN, Pederson MR, Kortus J (2000) Al_7CX (X = *Li*-Cs) clusters: Stability and the prospect for cluster materials. *Phys Rev B* 62:16956–16961.
67. Negishi Y, Kawamata H, Nakajima A, Kaya K (2000) Photoelectron spectroscopy of tin and lead cluster anions: Application of halogen-doping method. *J Electron Spectros Relat Phenomena* 106:117–125.
68. Cui LF, Wang L-S (2008) Stable icosahedral hollow cage clusters: Stannaspherene (Sn_{12}^{2-}) and plumbaspherene (Pb_{12}^{2-}). *Int Rev Phys Chem* 27:139–166.
69. Zhou B, Denning MS, Kays DL, Goicoechea JM (2009) Synthesis and isolation of $[Fe@Ge_{10}]^{3-}$: A pentagonal prismatic Zintl ion cage encapsulating an interstitial iron atom. *J Am Chem Soc* 131:2802–2803.
70. Wang J-Q, Stegmaier S, Fässler TF (2009) $[Co@Ge_{10}]^{3-}$—an intermetalloid cluster with Archimedean pentagonal prismatic structure. *Angew Chem Int Ed Engl* 48:1998–2002.
71. Koyasu K, Akutsu M, Atobe J, Mitsui M, Nakajima A (2006) Electronic properties of Cs-atom doped aluminum and silicon clusters: Al_nCs_m and Si_nCs_m. *Chem Phys Lett* 421:534–539.
72. Corbett JD (1985) Polyatomic Zintl anions of the post-transition elements. *Chem Rev* 85:383–397.
73. Eichhorn B, Kocak FS (2011) Dynamic properties of the group 14 Zintl ions and their derivatives. *Struct Bonding* 140:59–89.
74. Gupta U, et al. (2008) Effect of charge and composition on the structural fluxionality and stability of nine atom tin-bismuth Zintl analogues. *Inorg Chem* 47:10953–10958.
75. Melko JJ, et al. (2010) Anion photoelectron spectroscopy and first-principles study of Pb_xIn_y clusters. *J Phys Chem C* 114:20907–20916.
76. Kesanli B, et al. (2007) Cluster growth and fragmentation in the highly fluxional platinum derivatives of Sn_9^{4-}: Synthesis, characterization, and solution dynamics of $Pt_2@Sn_{17}^{4-}$ and $Pt@Sn_9H^{3-}$. *J Am Chem Soc* 129:4567–4574.
77. Esenturk EN, Fettinger JC, Eichhorn BW (2006) Synthesis, structure, and dynamic properties of $[Ni_2Sn_{17}]^{4-}$. *J Am Chem Soc* 128:12–13.
78. Kocak FS, Zavalij P, Lam YF, Eichhorn BW (2008) Solution dynamics and gas phase chemistry of $Pd_2@Sn_{18}^{4-}$. *Inorg Chem* 47:3515–3520.